



ATLAS CONF Note

ATLAS-CONF-2020-047

29th July 2020



Search for squarks and gluinos in final states with an isolated lepton, jets, and missing transverse momentum at $\sqrt{s} = 13$ TeV with the ATLAS detector

The ATLAS Collaboration

The results of a search for gluino and squark pair production $pp \rightarrow \tilde{q}\tilde{q}$, $pp \rightarrow \tilde{g}\tilde{g}$ decaying via charginos ($\tilde{\chi}_1^\pm$) to a final state consisting of a W boson, the lightest neutralino ($\tilde{\chi}_1^0$), and quarks are presented. The signal is characterized by the presence of a single charged lepton from a W boson decay, jets, and missing transverse momentum. The analysis was performed using proton-proton collision data taken at a center-of-mass energy $\sqrt{s} = 13$ TeV provided by the Large Hadron Collider and recorded by the ATLAS experiment, corresponding to 139 fb^{-1} . No statistically significant excess of events above the Standard Model expectation is found. Limits are set on the direct production of squarks and gluino in the simplified models: masses of \tilde{g} (\tilde{q}) up to 2.2 TeV (1.4 TeV) are excluded at 95% confidence level.

1 Introduction

While the Standard Model (SM) has proven to be a very successful theory, it is not a complete description of nature: the discovery of the SM Higgs boson [1–4], achieved by the ATLAS and CMS collaborations, confirmed the predicted electroweak symmetry breaking, but highlighted the hierarchy problem [5–8]. Supersymmetry (SUSY) [9–14] is a theoretical framework which assumes supersymmetric particles (gluino/squark) differing from their SM partners by a half unit of spin. By introducing a new fermionic (bosonic) supersymmetric partner for each boson (fermion) in the SM, SUSY provides a possible solution to the hierarchy problem. In SUSY models conserving R -parity [15], gluinos/squarks are produced in pairs. The lightest supersymmetric particle (LSP) has to be stable and is possibly weakly interacting, constituting a viable dark-matter candidate [16, 17].

The partner particles of the SM fermions (quarks and leptons) are the scalar squarks (\tilde{q}) and sleptons ($\tilde{\ell}$). In the boson sector, the supersymmetric partner of the gluon is the fermionic gluino (\tilde{g}). The supersymmetric partners of the Higgs (higgsinos) and of the electroweak gauge bosons (winos and bino) mix to form charged mass eigenstates (charginos) and neutral mass eigenstates (neutralinos). In the minimal supersymmetric extension of the Standard Model (MSSM) [18, 19] two scalar Higgs doublets along with their higgsino partners are necessary, resulting in two charginos ($\tilde{\chi}_1^\pm$) and four neutralinos ($\tilde{\chi}_1^0, \tilde{\chi}_{2,3,4}^0$).

Squarks and gluinos, in R -parity conserving scenarios, can be produced in pairs through the strong interaction. If strongly interacting gluinos/squarks are present at the TeV-scale, they should be copiously produced in the 13 TeV pp collisions at the LHC. With the recorded integrated luminosity and the predicted cross-sections for squark and gluino production the searches are sensitive to sparticle masses of a few TeV.

This paper targets two simplified SUSY models [20, 21] describing the gluino and squark production processes and their decays. They serve as benchmark models and were first used in [22]. In these models, referred to as the gluino and squark one-step models, gluinos or squarks are produced in pairs: gluinos subsequently decay to a $\tilde{\chi}_1^\pm$ and two light quarks, while squarks decay to $\tilde{\chi}_1^\pm$ and one light quark. The $\tilde{\chi}_1^\pm$ further decay into a W boson and a $\tilde{\chi}_1^0$. The simplified model diagrams are shown in Figure 1. In the MSSM the decay chains are realised when $\tilde{\chi}_1^\pm$ is wino-like and $\tilde{\chi}_1^0$ is bino-like. In both models, the branching ratios for SUSY particles are assumed to be 100% for the aforementioned processes (squark/gluino to $\tilde{\chi}_1^\pm$ and quarks, and for $\tilde{\chi}_1^\pm \rightarrow \tilde{\chi}_1^0 W$). The SM particles are allowed to decay following their known branching fractions. All other sparticles, which do not explicitly appear in the decay chain, are set to be kinematically inaccessible and decoupled.

In this search two different types of mass spectra have been considered. In the first one, the $\tilde{\chi}_1^\pm$ mass is set to be exactly midway between the masses of the gluino (squark) and the $\tilde{\chi}_1^0$, so that the relative mass splitting $x = (m(\tilde{\chi}_1^\pm) - m(\tilde{\chi}_1^0)) / (m(\tilde{g}/\tilde{q}) - m(\tilde{\chi}_1^0))$ is equal to 1/2. In the second mass spectrum, the $\tilde{\chi}_1^0$ mass is set to be 60 GeV while the gluino (squark) mass and the relative mass splitting are free parameters.

The experimental signature of the models consists of a single lepton (electron or muon) produced by the leptonic decay of one of the W bosons, at least two jets, and large missing transverse momentum (E_T^{miss}) from an undetectable neutrino and neutralinos. The sparticle masses define the energy available in their decays; therefore the number of jets and their kinematic properties depend on the mass spectrum in the model of interest. Four signal regions with two, four and six jets are defined to provide sensitivity to a broad range of mass spectra in the gluino and squark one-step models.

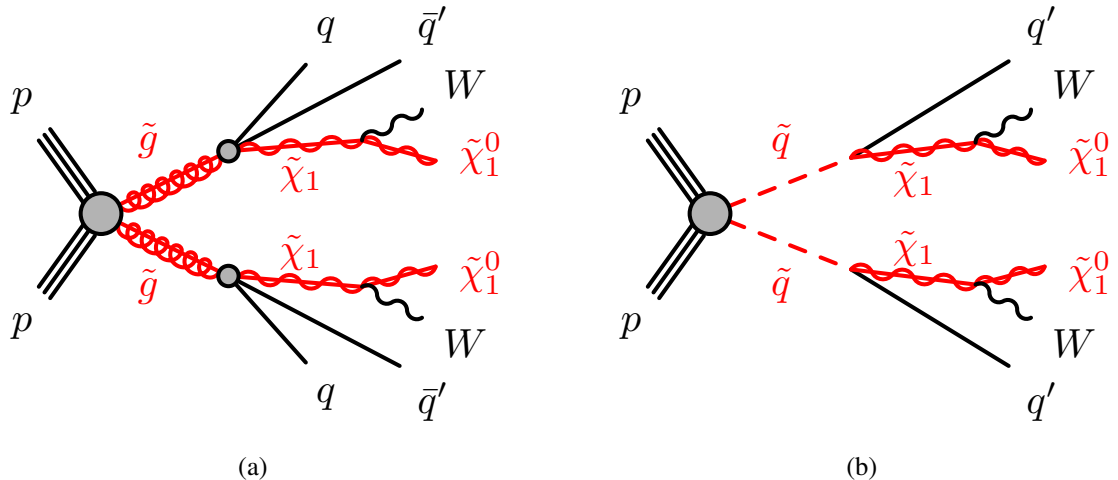


Figure 1: Diagrams for gluino (a) and squark(b) pair production with subsequent decays into quarks and a $\tilde{\chi}_1^\pm$. The $\tilde{\chi}_1^\pm$ further decays into a $\tilde{\chi}_1^0$ and a W boson. This analysis targets final states in which one W decays leptonically.

The results presented in this paper are based on the ATLAS data collected in proton–proton collisions at the LHC during 2015–2018 at a center-of-mass energy of 13 TeV, data corresponding to an integrated luminosity of 139 fb^{-1} . This analysis improves on previous ATLAS search with an integrated luminosity of 36.1 fb^{-1} [23]. Similar searches for gluinos and squarks with decays via intermediate supersymmetric particles were performed by the CMS Collaboration [24, 25].

2 ATLAS detector

The ATLAS detector [26–28] is a multipurpose particle detector with a nearly 4π coverage in solid angle.¹ It consists of an inner tracking detector surrounded by a thin superconducting solenoid providing a 2 T axial magnetic field, electromagnetic and hadron calorimeters, and a muon spectrometer. The inner tracking detector covers the pseudorapidity range $|\eta| < 2.5$. It consists of silicon pixel, silicon microstrip, and transition radiation tracking detectors. Lead/liquid-argon (LAr) sampling calorimeters provide electromagnetic (EM) energy measurements with high granularity. A steel/scintillator-tile hadron calorimeter covers the central pseudorapidity range ($|\eta| < 1.7$). The endcap and forward regions are instrumented with LAr calorimeters for EM and hadronic energy measurements up to $|\eta| = 4.9$. The muon spectrometer surrounds the calorimeters and is based on three large air-core toroidal superconducting magnets with eight coils each. The field integral of the toroids ranges between 2.0 and 6.0 Tm across most of the detector. The muon spectrometer includes a system of precision tracking chambers and fast detectors for triggering. A two-level trigger system [29] is used to select events. The first-level trigger is implemented in hardware and uses a subset of the detector information to keep the accepted rate below

¹ ATLAS uses a right-handed coordinate system with its origin at the nominal interaction point in the centre of the detector. The positive x -axis is defined by the direction from the interaction point to the centre of the LHC ring, with the positive y -axis pointing upwards, while the beam direction defines the z -axis. Cylindrical coordinates (r, ϕ) are used in the transverse plane, ϕ being the azimuthal angle around the z -axis. The pseudorapidity η is defined in terms of the polar angle θ by $\eta = -\ln(\tan(\theta/2))$. Rapidity is defined as $y = 0.5 \ln[(E + p_z)/(E - p_z)]$ where E denotes the energy and p_z is the component of the momentum along the beam direction. The angular distance ΔR is defined as $\sqrt{(\Delta y)^2 + (\Delta \phi)^2}$.

100 kHz. This is followed by a software-based trigger that reduces the accepted event rate to 1 kHz on average.

3 Dataset and simulated events

The search is performed using 139 fb^{-1} of pp LHC collision data collected between 2015 and 2018 by the ATLAS detector, with a centre-of-mass energy of 13 TeV and a 25 ns proton bunch crossing interval. In 2015–2016 the average number of interactions per bunch crossing (pile-up) was $\langle \mu \rangle = 20$, increasing to $\langle \mu \rangle = 38$ in 2017 and to $\langle \mu \rangle = 37$ in 2018. The uncertainty in the combined 2015–2018 integrated luminosity is 1.7% [30], obtained using the LUCID-2 detector [31] for the primary luminosity measurements.

The SM backgrounds modeling, signal selection efficiencies, and signal event yield are evaluated using Monte Carlo (MC) simulated event samples. All the samples are produced by a faster simulation [32] based on a parameterisation of the calorimeter response and GEANT 4 for the other detector systems or on ATLAS simulation infrastructure [33] and GEANT 4 [34].

To model the pile-up observed in data, inelastic pp events were generated with PYTHIA 8.186 [35] using the NNPDF2.3LO set of PDFs [36] and the A3 tune [37]. These events are overlaid to all simulated events to model the concurring proton–proton interaction in the same and nearby bunch crossings. The pile-up overlay is further reweighted to match the observed distribution in data. The simulated events are reconstructed with the same algorithms as those used for data.

The SUSY signal samples are produced with different generators depending on the process: gluino pair production is generated using MADGRAPH5_AMC@NLO v2.6.2 and PYTHIA 8.212; squark pair production samples are generated using MADGRAPH5_AMC@NLO v2.6.2 and PYTHIA 8.230. Signal cross-sections are calculated to approximate next-to-next-to-leading order in the strong coupling constant, adding the resummation of soft gluon emission at next-to-next-to-leading-logarithmic accuracy (approximate NNLO+NNLL) [38–45]. The nominal cross-section and the uncertainty are derived using the PDF4LHC15_mc PDF set, following the recommendations of Ref. [46]. A typical cross-section for gluino production with $m_{\tilde{g}} = 2000 \text{ GeV}$ and $m_{\tilde{\chi}_1^0} = 200 \text{ GeV}$ is $1.01 \pm 0.20 \text{ fb}$, while for squarks with $m_{\tilde{q}} = 1200 \text{ GeV}$ and $m_{\tilde{\chi}_1^0} = 200 \text{ GeV}$ a typical cross-section is $6.84 \pm 0.89 \text{ fb}$ when the four left-handed squarks of the first two generations ($\tilde{u}_L, \tilde{d}_L, \tilde{s}_L$, and \tilde{c}_L) are assumed to be mass-degenerate. A limit is also given assuming that only one such squark is kinematically accessible.

The SM backgrounds considered are: $t\bar{t}$ pair production; single-top production (s -channel, t -channel, and associated Wt production); $W/Z+\text{jets}$ production; $t\bar{t}$ production with an electroweak boson ($t\bar{t}V$); and diboson (WW, WZ, ZZ) production. Different MC event generators were used to produce the background samples, depending on their production process. The MC produced events are then normalised to data using the respective theoretical cross-sections. The event generators, the routines for parton showering and hadronization, and the parameter tunes and parton distribution functions for all background processes produced are summarised in Table 1.

$W+\text{jets}$ events are produced using SHERPA and the modeling includes up to two partons at NLO and four partons at LO using Comix [47] and OpenLoops [48, 49] in the matrix element which are merged with the SHERPA parton shower [50] according to the ME+PS@NLO prescription [51–54] using the set of tuned parameters developed by the SHERPA authors.

Table 1: Overview of MC generators used for different simulated event samples.

Process	Generator	Parton shower and hadronisation	Tune	PDF	Cross-section
$t\bar{t}$	POWHEG-Box v2 [57–60]	PYTHIA 8.230 [61]	A14 [62]	NNPDF2.3LO [36]	NNLO+NNLL [63]
Single top	POWHEG-Box v2 [64–66]	PYTHIA 8.230	A14	NNPDF2.3LO	NLO+NNLL [67]
W/Z -jets	SHERPA 2.2.1 [68]	SHERPA 2.2.1	SHERPA default	NNPDF3.0NNLO	NNLO [69]
Diboson	SHERPA 2.2.1 & 2.2.2	SHERPA 2.2.1 & 2.2.2	SHERPA default	NNPDF3.0NNLO	NLO
$t\bar{t} + V$	MG5_AMC@NLO v2.3.3	PYTHIA 8.210	A14	NNPDF2.3LO	NLO [70]

To simulate the properties of the bottom- and charm-hadron decays, the EvtGen v1.2.0 [55] program was used for all samples showered with PYTHIA .

Systematics uncertainties derived from the MC generator configuration are evaluated using samples produced without detector simulation. The uncertainties include variations of the renormalisation and factorisation scales, the CKKW-L [56] matching scale, as well as different PDF sets and fragmentation/hadronisation models. Details of the MC modelling uncertainties are discussed in Section 7.

4 Object reconstruction

Each event is required to have at least one reconstructed interaction vertex with a minimum of two associated tracks each having $p_T > 500$ MeV. In events with multiple vertices, the one with the highest sum of squared transverse momenta of associated tracks is chosen as the primary vertex (PV) [71]. A set of baseline quality criteria are applied to reject events with non-collision backgrounds or detector noise [72].

Two levels of object definition for leptons and jets are used: ‘baseline’ and ‘signal’. Loose quality requirements define baseline objects, which are used in the missing transverse momentum calculation and in the overlap removal procedure described below. Signal objects, as a subset of the baseline ones, are further selected with tighter identification criteria, and are used for defining the search regions. Selections over a list of track-based and calorimeter-based variables, employed as isolation criteria, are used to discriminate the signal leptons against semileptonic heavy-flavour decays and jets misidentified as leptons.

The energy deposits in the electromagnetic calorimeter matching to charged-particle tracks in the inner detector (ID) [73] provide electron candidates. Baseline electrons must have $p_T > 7$ GeV and $|\eta| < 2.47$, and satisfy the *loose* operating point provided by a likelihood-based algorithm, described in Ref. [73]. Electrons and converted photons are discriminated using the number of hits on the track. The longitudinal impact parameter z_0 ² relative to the PV is required to satisfy $|z_0 \sin \theta| < 0.5$ mm. Signal electron candidates are required to satisfy the *tight* likelihood operating point, with further criteria on the significance of the transverse impact parameter d_0 as $|d_0/\sigma(d_0)| < 5$. Signal electrons with $p_T < 200$ GeV are refined using the *Loose* isolation working point, while those with larger p_T are required to pass the *HighPtCaloOnly* isolation working point, as described in Ref. [73].

Muon candidates are reconstructed from matching tracks in the ID and muon spectrometer, refined through a global fit using the hits from both subdetectors [74]. Baseline muons are required to satisfy $p_T > 6$ GeV

² The transverse impact parameter is defined as the distance of closest approach in the transverse plane between a track and the beam-line. The longitudinal impact parameter corresponds to the z -coordinate distance between the point along the track at which the transverse impact parameter is defined and the primary vertex.

and $|\eta| < 2.7$. They are identified using the *medium* identification criteria. Similarly to electrons, the longitudinal impact parameter z_0 relative to the PV is required to satisfy $|z_0 \sin \theta| < 0.5$ mm. Signal muon candidates are further selected with tighter pseudorapidity and impact parameter requirements, $|\eta| < 2.5$ and $|d_0/\sigma(d_0)| < 3$ and have to satisfy the *FixedCutLoose* isolation working point requirements [74].

Jet candidates are reconstructed from three-dimensional topological energy clusters in the calorimeters using the anti- k_t algorithm [75] with a radius parameter $R = 0.4$ [76]. Baseline jets are defined in the region $|\eta| < 4.5$ and have $p_T > 20$ GeV. To suppress pile-up interactions, those jets having $|\eta| < 2.8$ and $p_T < 120$ GeV are required to pass the *medium* working point of the jet vertex tagger (JVT), a tagging algorithm that identifies jets originating from the PV using track information [77, 78]. Signal jets are further required to have $|\eta| < 2.8$ and to have $p_T > 30$ GeV.

‘*B*-tagged’ jets are enriched in *b*-hadrons, and are selected in the region $|\eta| < 2.5$ and with $p_T > 20$ GeV. They are identified as ‘*b*-tagged’ using the MV2c10 algorithm [79]. The *b*-tagging working point provides an efficiency of 77% for jets containing *b*-hadrons in simulated $t\bar{t}$ events, with rejection rates of 110 and 4.9 for light-flavour jets and jets containing *c*-hadrons, respectively [80].

An overlap removal procedure is applied to the baseline objects defined above to resolve the reconstruction ambiguities between electrons, muons and jets. Firstly, any electron sharing the same ID track with a muon is rejected. If two electrons share the same ID track, the one with lower p_T is discarded. Next, jets are rejected if they lie within $\Delta R = 0.2$ of an electron and then electrons are removed if they are within a shrinking cone of size $\Delta R = \min(0.4, 0.04 + 10 \text{ GeV}/p_T)$ around a jet. Subsequently, jets are rejected when they are close to a muon within $\Delta R = 0.2$ or if the muon is matched to the jet through ghost association [81]. Finally, muons within a cone, defined in the same way as for electrons, around any remaining jet are removed.

The missing transverse momentum $\mathbf{p}_T^{\text{miss}}$, with its magnitude E_T^{miss} , is calculated as the negative vectorial sum of the transverse momentum of all reconstructed baseline objects (electrons, muons, jets and photons [82]) and the soft term. The soft term includes all selected tracks associated with the PV but not matched to any reconstructed physics object. Tracks not associated with the PV are not accounted in the E_T^{miss} calculation, improving the E_T^{miss} resolution by suppressing the effect of pile-up [83, 84].

The efficiency differences in the trigger, particle identification and the reconstruction between data and simulated events are closely evaluated in independent measurements, and are accounted for by applying the corresponding corrections to the simulation in this analysis.

5 Event selection

Events satisfying the E_T^{miss} trigger selection are recorded [85]. The trigger is $> 98\%$ efficient for offline E_T^{miss} values above 250 GeV. To target the signal-like events, selected events are required to have exactly one signal lepton, either an electron or a muon. The events with additional baseline leptons are rejected to suppress the dilepton $t\bar{t}$, single-top (Wt -channel), Z -jets and diboson backgrounds. The following observables are used to further suppress background contributions and increase the sensitivity for signal:

- The transverse mass, m_T , is defined from the lepton transverse momentum \mathbf{p}_T^ℓ and $\mathbf{p}_T^{\text{miss}}$ as

$$m_T = \sqrt{2p_T^\ell E_T^{\text{miss}} (1 - \cos[\Delta\phi(\mathbf{p}_T^\ell, \mathbf{p}_T^{\text{miss}})])},$$

where $\Delta\phi(\mathbf{p}_T^\ell, \mathbf{p}_T^{\text{miss}})$ is the azimuthal angle between \mathbf{p}_T^ℓ and $\mathbf{p}_T^{\text{miss}}$. The observable has an upper endpoint at the W -boson mass, i.e. for W +jets and semileptonic $t\bar{t}$ events, in which one on-shell W boson decays leptonically. The m_T distribution for signal events extends significantly beyond the distributions of the W +jets and semileptonic $t\bar{t}$ events.

- The effective mass, m_{eff} , is the scalar sum of the p_T of the signal lepton and all signal jets and E_T^{miss} :

$$m_{\text{eff}} = p_T^\ell + \sum_{j=1}^{N_{\text{jet}}} p_{T,j} + E_T^{\text{miss}}.$$

The effective mass provides good discrimination against background events, especially for the signal scenarios with energetic jets. Gluino production can lead to higher jet multiplicity than can squark production. High-mass gluino/squark tend to produce harder jets than low-mass gluino/squark. Thus, the optimal m_{eff} value depends on the different signal scenarios. To achieve a wide-range sensitivity of various SUSY models with a limited number of signal regions, m_{eff} is binned instead of one single m_{eff} selection in the final model-dependent signal region.

- The aplanarity is a variable designed to provide more global information about the full momentum tensor of the event. It is defined as $(3/2) \times \lambda_3$, where λ_3 is the smallest eigenvalue of the sphericity tensor [86]. Typical measured aplanarity values lie in the range 0 – 0.3, with values near zero indicating relatively planar background-like events. Strongly produced SUSY signals tend to have high aplanarity values, since they are more spherical than background events due to the multiple objects emitted in the gluino/squark decay chains.

Four mutually exclusive signal regions (SRs) are designed to maximise the signal sensitivity. The selection criteria for the four SRs are summarised in Table 2. Each SR is optimised for specific SUSY scenarios as discussed below. They are labeled by the minimum required number of jets and, if relevant, the characteristics of the targeted supersymmetric mass spectrum: **2J**, **4J high-x**, **4J low-x**, and **6J**. For setting model-dependent exclusion limits (“excl”), each SR is further binned in b -veto/ b -tag and m_{eff} , and a simultaneous fit is performed across all bins of the four SRs. This choice enhances the sensitivity to a range of new-physics scenarios with or without b -quarks in the final states, and with different mass separations between the supersymmetric particles. For model-independent limits and null-hypothesis tests (“disc” for discovery), the event yield in each SR is used to search for an excess over the SM background using an optimised minimum value of m_{eff} . The systematic uncertainties, fit and results discussed in the following sections are based on the exclusion SRs, while the model-independent results are based on the discovery SRs.

The **2J** SR targets compressed scenarios, where difference between $m_{\tilde{g}/\tilde{q}}$, $m_{\tilde{\chi}_1^\pm}$, and $m_{\tilde{\chi}_1^0}$ are small and the decay products tend to be low- p_T . Thus, events with one low- p_T lepton are required with at least two jets. The lower p_T^ℓ threshold is 7 (6) GeV for the electron (muon), and the upper p_T^ℓ threshold increases with the jet multiplicity up to 25 GeV. The upper p_T^ℓ requirement ensures the orthogonality between **2J** SR and other signal regions. The jet multiplicity dependence allows the balance between background rejection and signal acceptance: the leptons are more energetic for signals with increasing mass splittings. Stringent requirements are placed on E_T^{miss} and on $E_T^{\text{miss}}/m_{\text{eff}}$ to enhance the signal sensitivity by selecting signal events with boosted final-state neutralinos recoiling against energetic initial-state radiation (ISR) jets. Compared to other SRs, a less stringent lower bound on m_{eff} is preferred to target compressed scenarios.

The **4J high-x** SR provides sensitivity to models with a fixed $m_{\tilde{\chi}_1^0} = 60$ GeV and a high x value, i.e., $m_{\tilde{\chi}_1^\pm}$ and $m_{\tilde{g}/\tilde{q}}$ are relatively compressed. Events with four or five jets are selected for this scenario. The

Table 2: Overview of the selection criteria for the signal regions used for gluino/squark one-step models. The requirements only apply to the exclusion (discovery) SRs are marked with “excl”(“disc”). The ‘+’ indicates that overflow events are included in the last bin.

SR	2J	4J high-x	4J low-x	6J
N_ℓ			= 1	
p_T^ℓ [GeV]	$> 7(6)$ for $e(\mu)$ and $< \min(10 \cdot N_{\text{jet}}, 25)$	> 25	> 25	> 25
N_{jet}	≥ 2	4–5	4–5	≥ 6
E_T^{miss} [GeV]	> 400	> 300	> 300	> 300
m_T [GeV]	> 100	> 520	$150\text{--}520$	> 225
Aplanarity	-	> 0.01	> 0.01	> 0.05
$E_T^{\text{miss}}/m_{\text{eff}}$	> 0.25	> 0.2	> 0.2	-
$N_{b\text{-jet}}$ (excl)			$= 0$ for b -veto, ≥ 1 for b -tag	
m_{eff} [GeV] (excl)	3 bins $\in [700, 2500+]$	3 bins $\in [1000, 2800+]$	3 bins $\in [1000, 2800+]$	4 bins $\in [700, 3500+]$
$N_{b\text{-jet}}$ (disc)			b -veto	
m_{eff} [GeV] (disc)	$> 1900(1300)$ for gluino (squark)	> 2200	> 2200	$> 2800(2100)$ for gluino (squark)

mass splitting between $m_{\tilde{\chi}_1^\pm}$ and $m_{\tilde{\chi}_1^0}$ is large enough to produce a boosted W boson that further decays into a high- p_T lepton and a neutrino. Large m_T is, thus, the most distinguishing characteristic of this SR. Relatively soft jets are expected to be emitted from the gluino or squark decays. The SM background is further suppressed by tight requirements on E_T^{miss} , aplanarity, and $E_T^{\text{miss}}/m_{\text{eff}}$. Compared to the **2J** SR, a tighter m_{eff} selection is applied due to higher jet activity.

The **4J low-x** SR is optimised for models where $m_{\tilde{\chi}_1^0}$ is fixed to 60 GeV and $x \approx 0$, i.e., $m_{\tilde{\chi}_1^\pm}$ is close to $m_{\tilde{\chi}_1^0}$. The jet multiplicity requirement is the same as in **4J high-x** SR. In contrast to the high- x scenarios, the small mass splitting between $m_{\tilde{\chi}_1^\pm}$ and $m_{\tilde{\chi}_1^0}$ tends to give an off-shell W boson, leading to small m_T . To keep this SR orthogonal to the **4J high-x** SR, an upper bound is applied to m_T . Other than that, the requirements on m_{eff} , E_T^{miss} , aplanarity, and $E_T^{\text{miss}}/m_{\text{eff}}$ are identical to the ones used in **4J high-x** SR.

The **6J** SR targets signal scenarios with high gluino/squark mass, and is optimised for models with $x = 1/2$. Events are selected with one high- p_T lepton and at least six jets. Large aplanarity is required reflecting the heavy gluino/squark produced in the targeted signature. Tight requirements on m_T and E_T^{miss} are imposed to reduce the SM background. To achieve high sensitivity for a wide range of $m_{\tilde{g}/\tilde{q}}$, the fitted m_{eff} bins range from 700 GeV to larger than 3500 GeV.

6 Background estimation

The prediction of the SM background event yields in SRs represents a very important component of this analysis and is estimated using different approaches for dominant and minor backgrounds. In processes leading to final states with one isolated lepton, jets and missing transverse energy, the dominant backgrounds are given by $t\bar{t}$, single top and W +jets, while the minor backgrounds are represented by Z +jets, $t\bar{t}$ in association with a W or Z boson, and diboson (WW , WZ , ZZ) events. In order to estimate the contributions

of $t\bar{t}$, single top and W +jets processes in SRs, a set of dedicated control regions (CRs) is defined, as described below.

Three sets of CRs, **2J**, **4J**, **6J**, are defined for estimating the backgrounds in the signal regions **2J**, **4J high-x**, **4J low-x** and **6J**, respectively. They satisfy the criteria of high purity for the targeted background process and low signal contamination for the model of interest. The purity varies from 57% to 88% for the top backgrounds ($t\bar{t}$ and single top) in top CRs and from 73% to 92% for W +jets in W +jets CRs. Each of the CRs is defined close to the SR kinematic space, in order to reduce the theoretical and detector uncertainties from the extrapolation. The contributions of the top and W +jets backgrounds in the SRs are evaluated with a fit based on the profile likelihood method. The normalised background predictions are obtained in a simultaneous fit across all control regions, as described in the results section. The control regions for top and W +jets are presented in the Table 3. Events in the top control region require at least one b-tagged signal jet in the event, while W +jets control regions are assembled by vetoing all events containing any b-tagged signal jets. The CRs are crafted in the same way as signal regions, thus each CR is defined as a function of m_{eff} , with the same binning as the corresponding SR. This permits extrapolation from each b-tag/b-veto and m_{eff} bin in CRs to the corresponding bin in the SRs. The extrapolation from CRs to SRs is performed via the m_T variable, which is found to be well modeled in simulation as shown in Figure 2.

In order to validate the background fit results, a cross-check of the background estimates are performed in validation regions (VRs) situated between the SRs and the CRs in m_T , but orthogonal to both regions. The VRs are also defined as function of m_{eff} in the same way as the corresponding CRs and SRs, to ensure a m_{eff} -dependent validation. An exception is made for the last m_{eff} bin in the **6J** VRs, as the signal contamination would be too high. This bin is, thus, not considered. The VRs are not used to constrain the fit, they only verify the agreement between the normalised background predictions and the observed data. The VR definitions and the full graphical region illustration are depicted in Table 4 and Figure 3.

The contributions of the minor backgrounds, such as Z +jets, $t\bar{t}+V$ and diboson, are evaluated from simulation. The procedure consists of normalisation of the simulated event samples to theoretical cross-sections. No dedicated control regions for the diboson background were used, as the modelling of this background by simulation was found to be good as verified in the validation regions. The background originating from misidentified leptons, real leptons coming from jet produced by heavy-flavour quarks or photons converted to electrons was found to be insignificant due to the stringent requirements on E_T^{miss} .

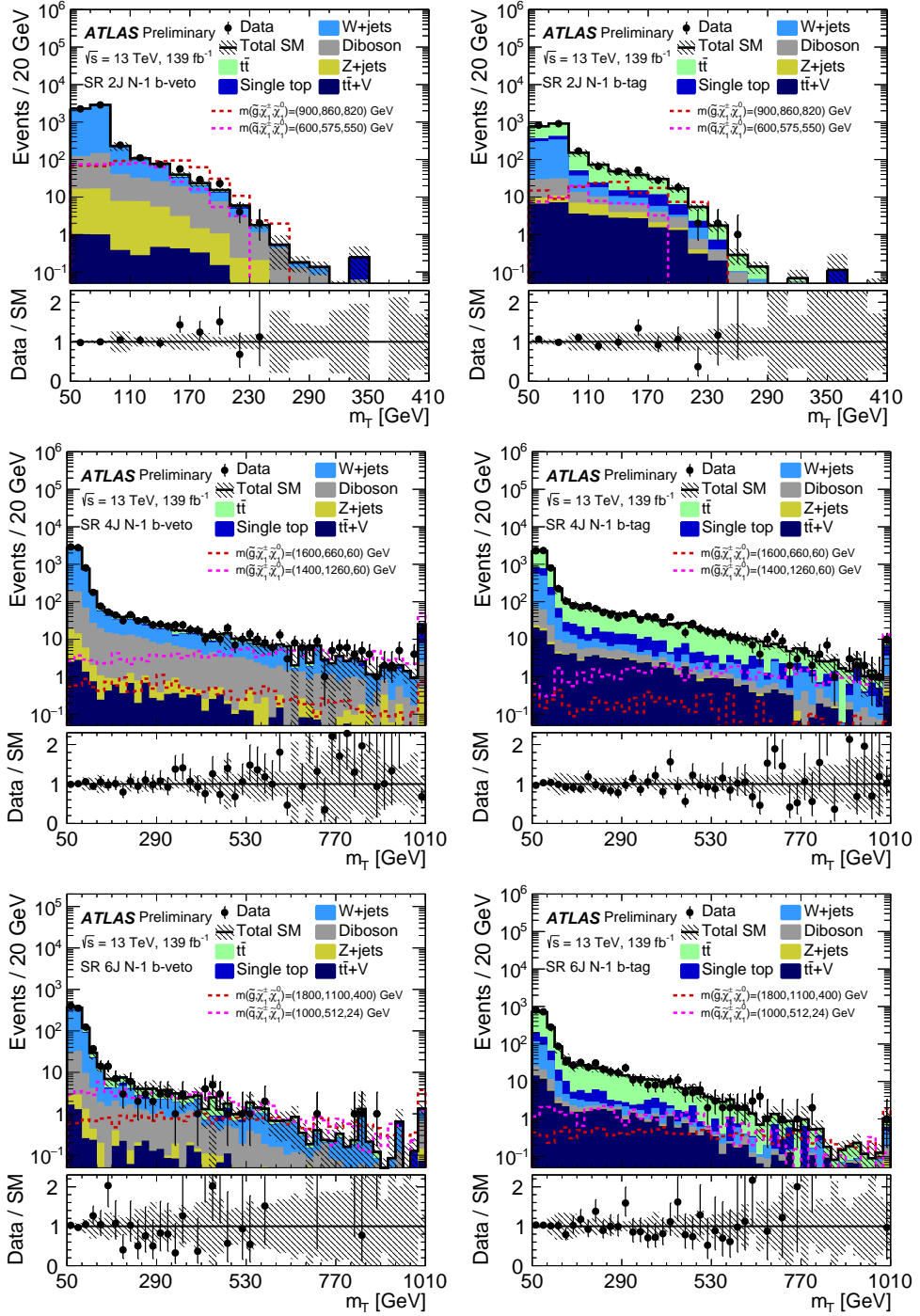


Figure 2: The m_T distributions in the signal regions after all of the selection requirements other than the m_T cut. Due to the removal of the m_T requirement, these plots effectively show the CRs, VRs and SRs in each jet multiplicity. The uncertainty bands include all statistical and systematic uncertainties. Overflow events are included in the last bin. The dashed lines represent benchmark signal points.

Table 3: Overview of the control region selection criteria. The top and W +jets control regions are denoted by b-tag and b-veto requirement, respectively.

CR	2J	4J	6J
N_ℓ		$= 1$	
p_T^ℓ [GeV]	$> 7(6)$ for $e(\mu)$ and $< \min(10 \cdot N_{\text{jet}}, 25)$	> 25	> 25
N_{jet}	≥ 2	4–5	≥ 6
E_T^{miss} [GeV]	> 400	> 300	> 250
m_T [GeV]	$50 - 80$	$50 - 90$	$50 - 100$
Aplanarity	-	> 0.01	> 0.05
$E_T^{\text{miss}}/m_{\text{eff}}$	> 0.25	> 0.2	-
m_{eff} [GeV]	3 bins $\in [700, 2500+]$	3 bins $\in [1000, 2800+]$	4 bins $\in [700, 3500+]$
$N_{b-\text{jet}}$	<i>b</i> -tag for top CR; <i>b</i> -veto for W +jets CR		

Table 4: Overview of the validation region selection criteria. The top and W +jets validation regions are denoted by b-tag and b-veto requirement, respectively.

VR	2J	4J	6J
N_ℓ		$= 1$	
p_T^ℓ [GeV]	$> 7(6)$ for $e(\mu)$ and $< \min(10 \cdot N_{\text{jet}}, 25)$	> 25	> 25
N_{jet}	≥ 2	4–5	≥ 6
E_T^{miss} [GeV]	> 400	> 300	> 250
m_T [GeV]	$80 - 100$	$90 - 150$	$100 - 225$
Aplanarity	-	> 0.01	> 0.05
$E_T^{\text{miss}}/m_{\text{eff}}$	> 0.25	> 0.2	-
m_{eff} [GeV]	3 bins $\in [700, 2500+]$	3 bins $\in [1000, 2800+]$	3 bins $\in [700, 2800+]$
$N_{b-\text{jet}}$	<i>b</i> -tag for top VR; <i>b</i> -veto for W +jets VR		

As a representative example the m_{eff} distributions in **6J** top and W +jets control regions are shown in Figure 4 before and after a fit which constraints only the control regions. The fit strategy is discussed in details in Sec. 8. A trend is observed towards the large m_{eff} values between the data and the background expectation in the pre-fit kinematics. This is accounted for by applying different normalisation parameters for each m_{eff} bin in the fit, which effectively corrects the trend over the m_{eff} bins. In the after fit distributions, the data and the background expectation agree well within the uncertainties with the above fit construction.

7 Systematic uncertainties

The expected yields for both signal and background events are subject to two classes of uncertainties, experimental and theoretical. The various theoretical uncertainties for the main backgrounds influence

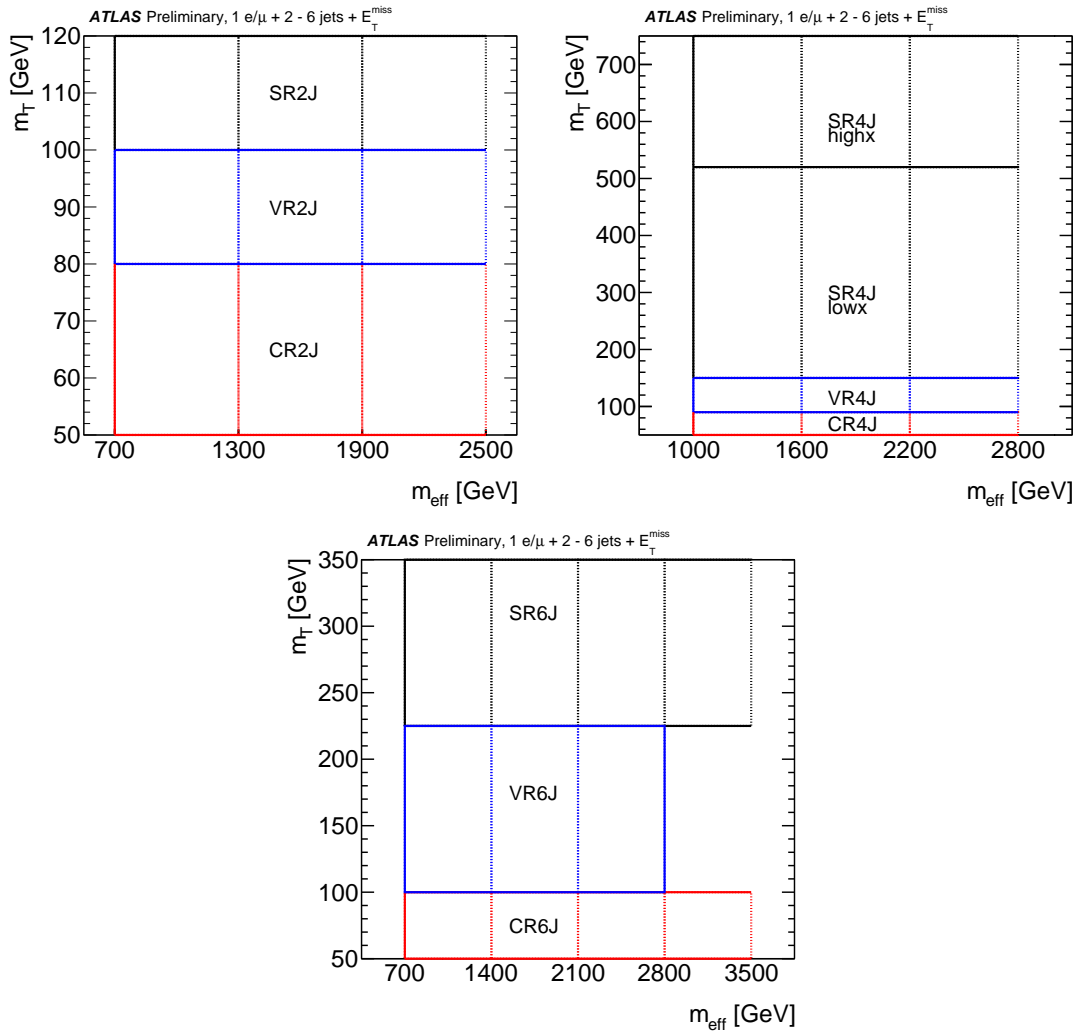


Figure 3: Graphical illustration of the control and validation region configuration corresponding to the 2J, 4J, 6J signal region. The variables shown on the x and y axes indicate other selections that differ between the corresponding control regions, validation regions and signal regions.

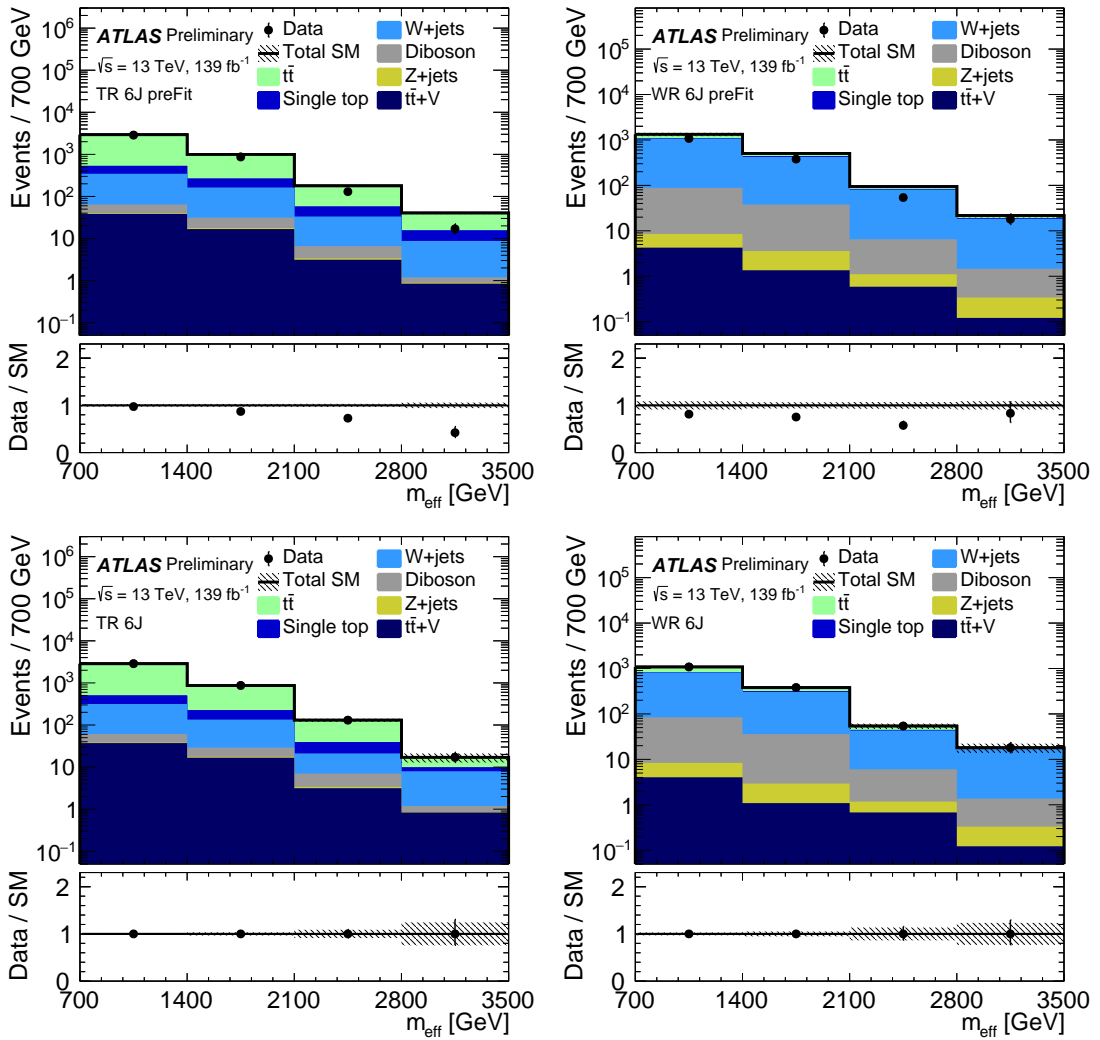


Figure 4: The m_{eff} distribution in **6J** top (left, noted as “TR”) and W +jets (right, noted as “WR”) control regions before (top) and after (bottom) fit. The uncertainty bands plotted include all statistical and systematic uncertainties. Overflow events are included in the last bin.

only the transfer factors from CR(s) to VR(s) and SR(s), while for the minor backgrounds, the uncertainties affect the inclusive cross-section of each process and the acceptance of the analysis selection.

Following the procedure from Sec. 6, the theoretical uncertainties are computed for each m_{eff} bin. For the single-top and $t\bar{t}$ backgrounds, the theoretical uncertainties due to hadronisation/fragmentation are estimated by comparing the predictions obtained with the Powheg-Box generator interfaced with two different parton shower generators, Pythia 8 and Herwig 7 [87], while the ones derived from hard-scattering are evaluated by a Powheg-Box +Pythia 8 and AMC@NLO +Pythia 8 comparison. Diagram removal (DR) and diagram subtraction (DS) samples, modelled by Powheg-Box +Pythia 8, are used to determine the impact of the interference between single-top Wt and $t\bar{t}$ production [88]. In order to evaluate the impact of the uncertainties coming from the emission of initial- and final-state radiation, the renormalisation, factorisation scales and showering are varied.

Table 5: Breakdown of the dominant systematic uncertainties on background estimates in the various signal regions. Note that the individual uncertainties can be correlated, and do not necessarily add up quadratically to the total background uncertainty. The percentages show the size of the uncertainty relative to the total expected background.

Uncertainty of channel	2J b-veto	2J b-tag	4J low-x b-veto	4J low-x b-tag
Total background expectation	346	272	449	810
Total background systematic	8%	25%	7%	13%
W+jets theo. uncert.	0.6%	1.8%	1.6%	0.9%
Jet Energy Resolution	2.5%	4%	2.9%	2.4%
MC statistics	3.0%	1.5%	1.6%	0.8%
$t\bar{t}$ theo. uncert.	5%	23%	3.1%	12%
Lepton uncertainties	1.0%	0.6%	0.5%	0.34%
Jet Energy Scale	1.8%	1.6%	2.4%	1.5%
Normalisation of dominant backgrounds	1.5%	9%	1.0%	4%
Other theo. uncert.	2.7%	0.8%	2.8%	0.26%
B-tagging	1.6%	1.7%	2.2%	1.3%
MET/JVT/pile-up/trigger	1.9%	0.3%	0.5%	0.6%
single top theo. uncert.	0.7%	4%	0.9%	1.3%

The uncertainties for $t\bar{t} + V$, $W/Z + \text{jets}$ and dibosons coming from scale variations have been evaluated by considering the envelope of the seven-point variations of the renormalisation and factorisation scales. The resummation (QSF) and matrix element matching (CKKW) variations for $W/Z + \text{jets}$ are estimated by varying up and down by a factor of 2 with respect to the nominal scale for each region. The PDF uncertainties for $W/Z + \text{jets}$ are considered and following the recommendation in PDF4LHC15 [46], while the ones for $t\bar{t}$ were found negligible in all the regions. Values of 5% and 6% systematic uncertainty in the inclusive cross-section for $t\bar{t} + V$ and diboson processes are assigned, respectively. For the other small background processes such as $Z + \text{jets}$, the systematic uncertainty in the inclusive cross section is included at the 5% level.

The theoretical uncertainties in the expected yields for the two signal models are considered and estimated using MG5_AMC@NLO +PYTHIA 8 samples by varying the parameters corresponding to the factorisation, renormalisation and CKKW-L matching scales.

The second categories of the uncertainties, the detector-related systematic uncertainties, consist of the jet energy scale (JES), the jet energy resolution (JER), lepton reconstruction and identification, b -tagging uncertainties, the E_T^{miss} modelling and the pile-up, as well as uncertainties on the trigger. The JES and JER represent the most dominant experimental systematics and are derived as a function of p_T and η of the jet, the pile-up conditions and the jet flavour composition [89]. The uncertainties on the lepton identification, momentum/energy scale and resolution are estimated from samples of $Z \rightarrow \ell^+\ell^-$, $J/\psi \rightarrow \ell^+\ell^-$ and $W \rightarrow \ell\nu$ decays [73, 74]. The E_T^{miss} modelling systematic uncertainties are evaluated by taking into account the uncertainties on the energy and momentum scale of each object used in the calculation, as well as the uncertainties on the soft term resolution and scale. The uncertainty on pile-up is computed by varying up and down the reweighting factor by $\pm 4\%$. Uncertainties due to the b -tagging efficiency are derived from data-driven measurements in $t\bar{t}$ events [79, 90], while uncertainties associated with the probability of

Table 6: Breakdown of the dominant systematic uncertainties on background estimates in the various signal regions. Note that the individual uncertainties can be correlated, and do not necessarily add up quadratically to the total background uncertainty. The percentages show the size of the uncertainty relative to the total expected background.

Uncertainty of channel	4J high-x b-veto	4J high-x b-tag	6J b-veto	6J b-tag
Total background expectation	117	160	46	196
Total background systematic	25%	17%	22%	15%
W+jets theo. uncert.	19%	7%	13%	0.5%
Jet Energy Resolution	12%	2.2%	10%	2.5%
MC statistics	5%	2.2%	4%	1.4%
$t\bar{t}$ theo. uncert.	5%	14%	17%	13%
Lepton uncertainties	4%	2.8%	1.2%	0.7%
Jet Energy Scale	2.0%	1.9%	4%	1.0%
Normalisation of dominant backgrounds	1.8%	3.1%	2.9%	3%
Other theo. uncert.	1.8%	0.30%	2.4%	0.16%
B-tagging	1.6%	1.8%	3.4%	0.8%
MET/JVT/pile-up/trigger	1.2%	0.8%	0.8%	0.8%
single top theo. uncert.	0.4%	3.2%	0.9%	4%

mistakenly b -tagging a jet which does not contain a b -hadron are determined using dijet samples [91].

Tables 5 and 6 detail the size of the different systematic uncertainties in the signal regions, summing over all m_{eff} bins. The uncertainty on the hard-scattering for $t\bar{t}$ dominates in many regions. Jet-related uncertainties dominate for detector-related uncertainties.

8 Results

The statistical interpretation is based on a profile likelihood method using the HistFitter framework [92]. The likelihood function consists of Poisson functions representing the control and signal regions. These Poisson functions depend on the observed number of data events in the respective region and the expected numbers of signal and background events. Different parameters are included in the likelihood function to control the normalisation of the backgrounds and the signal or to reflect statistical and systematic uncertainties. The normalisations of the major backgrounds, such as $t\bar{t}$, single-top and W +jets, are controlled by one normalisation factor for $t\bar{t}$ and single-top and another one for W +jets processes per jet multiplicity and m_{eff} range. This configuration corrects for the mismodelling of the m_{eff} distribution in the Monte Carlo simulation, as discussed in Section 6. An exception is made for the 4J case and $m_{\text{eff}} \in [1600, \infty)$ GeV, where only one normalisation factor is used for $t\bar{t}$ and single-top, in contrast, the yields in the control regions are sufficient to allow two normalisation factors for W +jets, one in the range $m_{\text{eff}} \in [1600, 2200]$ GeV and one for $m_{\text{eff}} \in [2200, \infty)$ GeV. In total, the fit thus includes nine normalisation factors for $t\bar{t}$ and single top and 10 normalisation factors for W +jets. The normalisation of the signal is controlled by one common normalisation factor in all bins included in the fit. Systematic uncertainties are accommodated through the use of nuisance parameters which are constrained by a Gaussian auxiliary term added to the likelihood.

Table 7: Event yields and background-only fit results for the 2J SRs for an integrated luminosity of 139 fb^{-1} . Each column corresponds to a bin in $m_{\text{eff}}[\text{GeV}]$. Uncertainties in the fitted background estimates combine statistical (in the simulated event yields) and systematic uncertainties. The uncertainties in this table are symmetrized for propagation purposes but are truncated at zero to remain within the physical boundaries.

2J b-veto	bin 1 [700,1300]	bin 2 [1300,1900]	bin 3 >1900 [GeV]
Observed events	280	84	22
Total SM background events	261 ± 22	73 ± 12	12.8 ± 2.2
$t\bar{t}$ events	19 ± 13	11 ± 7	1.3 ± 0.6
$W+\text{jets}$ events	155 ± 14	28 ± 5	3.4 ± 1.5
$Z+\text{jets}$ events	14 ± 5	4.3 ± 0.6	1.37 ± 0.18
single-top events	5 ± 4	2.9 ± 2.3	1.1 ± 0.9
diboson events	66 ± 8	26.0 ± 3.4	5.5 ± 0.7
$t\bar{t}+\text{V}$ events	1.32 ± 0.16	0.47 ± 0.23	0.041 ± 0.018
2J b-tag	bin 1 [700,1300]	bin 2 [1300,1900]	bin 3 >1900 [GeV]
Observed events	154	106	21
Total SM background	134 ± 36	123 ± 33	16 ± 6
$t\bar{t}$ events	74 ± 35	90 ± 32	10 ± 5
$W+\text{jets}$ events	20 ± 6	6.3 ± 2.1	0.7 ± 0.5
$Z+\text{jets}$ events	5.0 ± 0.7	2.0 ± 2.0	0.55 ± 0.09
single-top events	18 ± 7	15 ± 6	2.6 ± 1.6
diboson events	9.0 ± 1.4	4.3 ± 1.5	1.04 ± 0.17
$t\bar{t}+\text{V}$ events	8.4 ± 0.7	5.0 ± 0.5	0.63 ± 0.09

In a background-only fit, only the control regions are used to constrain the likelihood. A signal contribution is neglected in this fit, and consequently the signal normalisation parameter dropped. The observed yields in the VRs were found to be compatible with the background expectation obtained from this fit, with the largest statistical significance over the 18 bins being about 2σ . Background predictions in the signal regions are compared to the observed data in Tables 7-10 and illustrated in Figures 5-7. No significant data excess over background predictions is observed.

Using the discovery signal regions defined in Table 2, a test is performed for the presence of BSM physics in a model independent fit in each signal region. Signal contribution is only considered in the respective signal region, but not in the CRs, therefore a conservative background estimate is obtained in the signal regions. Table 11 shows the observed and expected upper limit on the signal events (S_{obs}^{95} and S_{exp}^{95}) at 95% confidence level (CL) using the CLs prescription [93]. Additionally reported is the visible cross-section upper limit ($\langle\epsilon\sigma\rangle_{\text{obs}}^{95}$), which is the upper limit on the cross-section times the reconstruction efficiency and region acceptance. The table also presents the discovery p-values (p_0), which quantify the probability to observe equal or more data assuming the background-only assumption, and the associated significance.

Observed and expected exclusion limits at 95% CL are calculated for the gluino and squark one-step models using all statistically independent binned signal and control regions in a model-dependent fit. For this exclusion fit, the signal contribution, adjusted using a single floating normalization factor, is considered in

Table 8: Event yields and background-only fit results for the 4J low- x SRs for an integrated luminosity of 139 fb^{-1} . Each column corresponds to a bin in $m_{\text{eff}}[\text{GeV}]$. Uncertainties in the fitted background estimates combine statistical (in the simulated event yields) and systematic uncertainties. The uncertainties in this table are symmetrized for propagation purposes but are truncated at zero to remain within the physical boundaries.

4J low-x b-veto	bin 1 [1000,1600]	bin 2 [1600,2200]	bin 3 $> 2200 \text{ [GeV]}$
Observed events	393	57	10
Total SM background	383 ± 27	56 ± 6	9.5 ± 1.7
$t\bar{t}$ events	72 ± 15	8.7 ± 1.8	1.56 ± 0.35
$W+\text{jets}$ events	179 ± 22	23 ± 4	3.4 ± 1.4
$Z+\text{jets}$ events	4.7 ± 0.8	0.73 ± 0.18	0.16 ± 0.04
single-top events	12 ± 5	3.3 ± 1.3	$0.16^{+0.25}_{-0.16}$
diboson events	110 ± 15	20.5 ± 2.8	4.2 ± 0.6
$t\bar{t}+V$ events	5.6 ± 0.6	0.54 ± 0.22	0.070 ± 0.031
4J low-x b-tag	bin 1 [1000,1600]	bin 2 [1600,2200]	bin 3 $> 2200 \text{ [GeV]}$
Observed events	695	79	11
Total SM background	701 ± 90	94 ± 19	15 ± 4
$t\bar{t}$ events	510 ± 90	60 ± 18	9.0 ± 2.9
$W+\text{jets}$ events	36 ± 9	7.0 ± 1.6	0.96 ± 0.35
$Z+\text{jets}$ events	1.7 ± 0.5	0.36 ± 0.08	0.035 ± 0.020
single-top events	88 ± 12	19 ± 6	3.9 ± 2.5
diboson events	21.1 ± 3.2	4.3 ± 0.6	0.90 ± 0.13
$t\bar{t}+V$ events	41.5 ± 3.0	3.9 ± 0.6	0.45 ± 0.10

all control and signal regions. The background normalization factors are simultaneously determined in the same fit. Specific sparticle masses in the gluino or squark one-step models can be excluded if the upper limit of the signal normalization factor is less than unity.

Figure 8 shows the expected and observed exclusion limits. Gluino masses up to 2.2 TeV and squark masses up to 1.37 TeV can be excluded for low mass $\tilde{\chi}_1^0$. Benefiting from the increased integrated luminosity, the current observed limit exceeds the previous ATLAS limit by about 100 GeV in $m_{\tilde{g}}$ and in $m_{\tilde{q}}$ for low mass $\tilde{\chi}_1^0$. Assuming a one-flavour scheme for the squark one-step model, squark masses around 1.0 TeV can be excluded.

Table 9: Event yields and background-only fit results for the 4J high-x SRs for an integrated luminosity of 139 fb^{-1} . Each column corresponds to a bin in $m_{\text{eff}}[\text{GeV}]$. Uncertainties in the fitted background estimates combine statistical (in the simulated event yields) and systematic uncertainties. The uncertainties in this table are symmetrized for propagation purposes but are truncated at zero to remain within the physical boundaries.

4J high-x b-veto	bin 1 [1000,1600]	bin 2 [1600,2200]	bin 3 $> 2200 \text{ [GeV]}$
Observed events	104	32	11
Total SM background	92 ± 32	18 ± 4	7.1 ± 2.3
$t\bar{t}$ events	9 ± 5	1.2 ± 0.4	0.32 ± 0.11
$W+\text{jets}$ events	61 ± 30	9 ± 4	3.6 ± 1.7
$Z+\text{jets}$ events	1.5 ± 0.6	0.8 ± 0.4	0.26 ± 0.14
single-top events	$0.3^{+0.5}_{-0.3}$	$0.006^{+0.026}_{-0.006}$	1.3 ± 0.8
diboson events	18.7 ± 2.9	6.1 ± 0.9	1.59 ± 0.29
$t\bar{t}+V$ events	0.65 ± 0.15	$0.09^{+0.13}_{-0.09}$	0.029 ± 0.023
4J high-x b-tag	bin 1 [1000,1600]	bin 2 [1600,2200]	bin 3 $> 2200 \text{ [GeV]}$
Observed events	121	26	8
Total SM background	127 ± 27	25 ± 5	7.7 ± 2.1
$t\bar{t}$ events	90 ± 24	13.1 ± 2.8	2.0 ± 0.5
$W+\text{jets}$ events	17 ± 9	4.6 ± 2.4	1.1 ± 0.4
$Z+\text{jets}$ events	0.32 ± 0.10	$0.01^{+0.13}_{-0.01}$	0.15 ± 0.09
single-top events	10 ± 4	4.9 ± 1.8	3.6 ± 1.7
diboson events	3.1 ± 0.6	1.20 ± 0.34	0.41 ± 0.15
$t\bar{t}+V$ events	5.8 ± 0.5	1.51 ± 0.17	0.39 ± 0.08

Table 10: Event yields and background-only fit results for the 6J SRs for an integrated luminosity of 139 fb^{-1} . Each column corresponds to a bin in $m_{\text{eff}}[\text{GeV}]$. Uncertainties in the fitted background estimates combine statistical (in the simulated event yields) and systematic uncertainties. The uncertainties in this table are symmetrized for propagation purposes but are truncated at zero to remain within the physical boundaries.

6J b-veto	bin 1 [700,1400]	bin 2 [1400,2100]	bin 3 [2100,2800]	bin 4 $> 2800 \text{ [GeV]}$
Observed events	19	16	3	2
Total SM background	25 ± 8	15.9 ± 2.5	3.5 ± 0.5	1.8 ± 0.6
$t\bar{t}$ events	10 ± 6	4.6 ± 1.7	0.77 ± 0.26	0.09 ± 0.07
$W+\text{jets}$ events	7 ± 5	5.2 ± 1.5	1.2 ± 0.5	0.6 ± 0.4
$Z+\text{jets}$ events	$0.23^{+0.23}_{-0.23}$	0.25 ± 0.06	0.12 ± 0.05	0.060 ± 0.024
single-top events	$0.5^{+0.8}_{-0.5}$	$0.3^{+0.5}_{-0.3}$	0.0 ± 0.0	0.5 ± 0.4
diboson events	6.2 ± 1.4	5.2 ± 0.9	1.31 ± 0.26	0.52 ± 0.16
$t\bar{t}+V$ events	0.90 ± 0.17	0.47 ± 0.11	0.06 ± 0.04	$0.012^{+0.021}_{-0.012}$

6J b-tag	bin 1 [700,1400]	bin 2 [1400,2100]	bin 3 [2100,2800]	bin 4 $> 2800 \text{ [GeV]}$
Observed events	117	68	7	2
Total SM background	110 ± 17	70 ± 11	13.6 ± 3.1	2.4 ± 1.0
$t\bar{t}$ events	90 ± 17	52 ± 10	10.2 ± 2.8	0.9 ± 0.6
$W+\text{jets}$ events	2.0 ± 1.3	1.6 ± 0.8	0.53 ± 0.16	0.46 ± 0.19
$Z+\text{jets}$ events	$0.05^{+0.09}_{-0.05}$	0.12 ± 0.04	0.06 ± 0.04	0.08 ± 0.04
single-top events	4.6 ± 3.1	9 ± 5	1.3 ± 1.1	$0.6^{+0.8}_{-0.6}$
diboson events	1.62 ± 0.32	1.64 ± 0.31	0.57 ± 0.13	0.14 ± 0.07
$t\bar{t}+V$ events	11.5 ± 1.5	5.1 ± 0.7	0.95 ± 0.24	0.20 ± 0.13

Table 11: Results of the model-independent limit fits. For each SR defined in Table 2, the observed events and the total SM background, the observed 95% CL upper limits on the visible cross section $\langle \epsilon\sigma \rangle_{\text{obs}}^{95}$ and on the number of signal events S_{obs}^{95} is given. The third column, S_{exp}^{95} , shows the 95% CL upper limit on the number of signal events, given the expected number (and $\pm 1\sigma$ excursions on the expectation) of background events. The last two columns indicate the CL_B value, i.e. the confidence level observed for the background-only hypothesis, the discovery p -value $p(s = 0)$ and the significance Z .

SR_{disc}	Observed events	Total SM background	$\langle \epsilon\sigma \rangle_{\text{obs}}^{95} [\text{fb}]$	S_{obs}^{95}	S_{exp}^{95}	CL_B	$p(s = 0) (Z)$
2J (gluino)	22	12.8 ± 2.2	0.14	19.0	$10.1^{+4.0}_{-2.3}$	0.98	0.02 (1.97)
2J (squark)	106	85 ± 12	0.34	47.7	30^{+13}_{-7}	0.91	0.09 (1.35)
4J high-x	11	7.1 ± 2.3	0.09	12.0	$8.3^{+3.5}_{-1.5}$	0.87	0.13 (1.12)
4J low-x	10	9.5 ± 1.7	0.06	8.9	$8.4^{+3.3}_{-2.0}$	0.57	0.42 (0.19)
6J (gluino)	2	1.8 ± 0.6	0.03	4.7	$4.3^{+1.9}_{-0.8}$	0.59	0.41 (0.24)
6J (squark)	5	5.3 ± 0.8	0.04	6.0	$6.0^{+24.0}_{-1.5}$	0.48	0.50 (0)

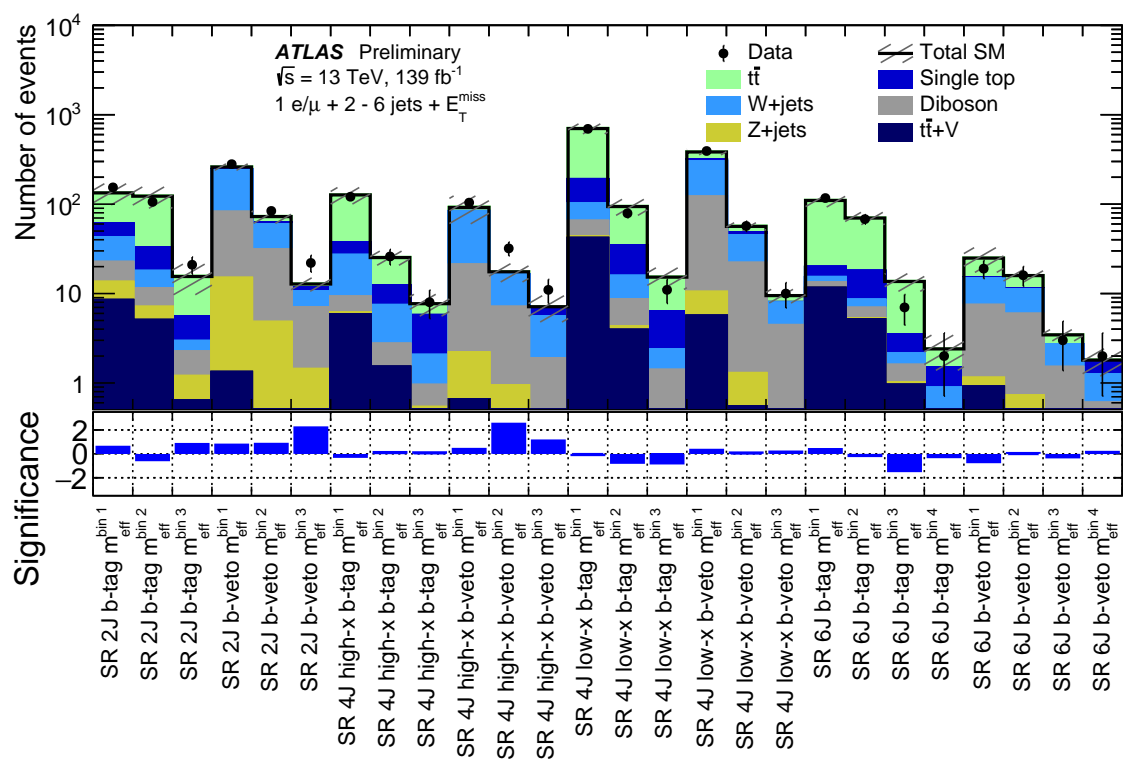


Figure 5: Comparison of the observed and expected event yields in all signal regions in the background-only fit.

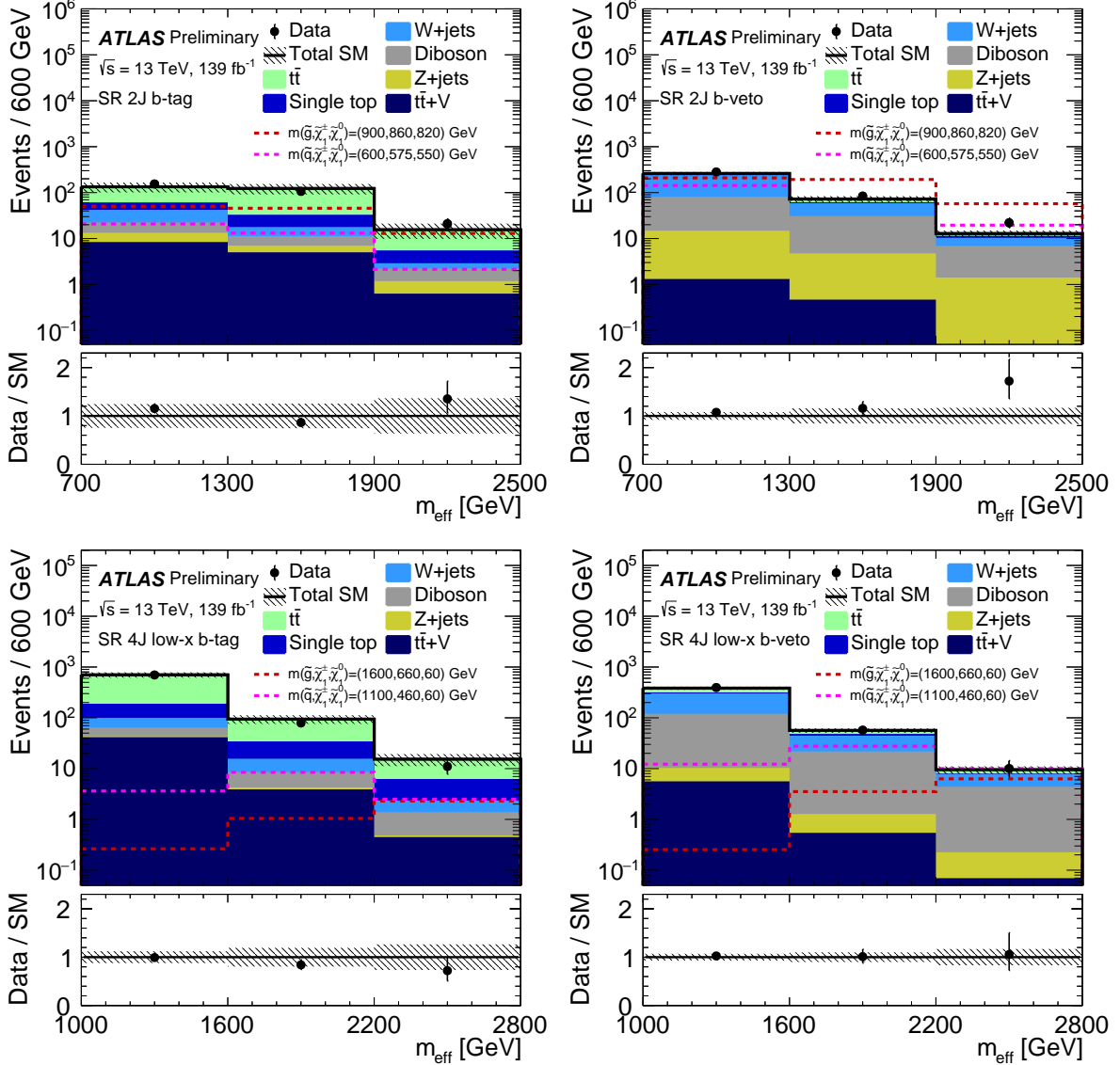


Figure 6: Post-fit m_{eff} distributions in the exclusion 2J and 4J low- x signal regions. The uncertainty bands include all statistical and systematic uncertainties. The dashed lines represent benchmark signal points. Overflow events are included in the last bin.

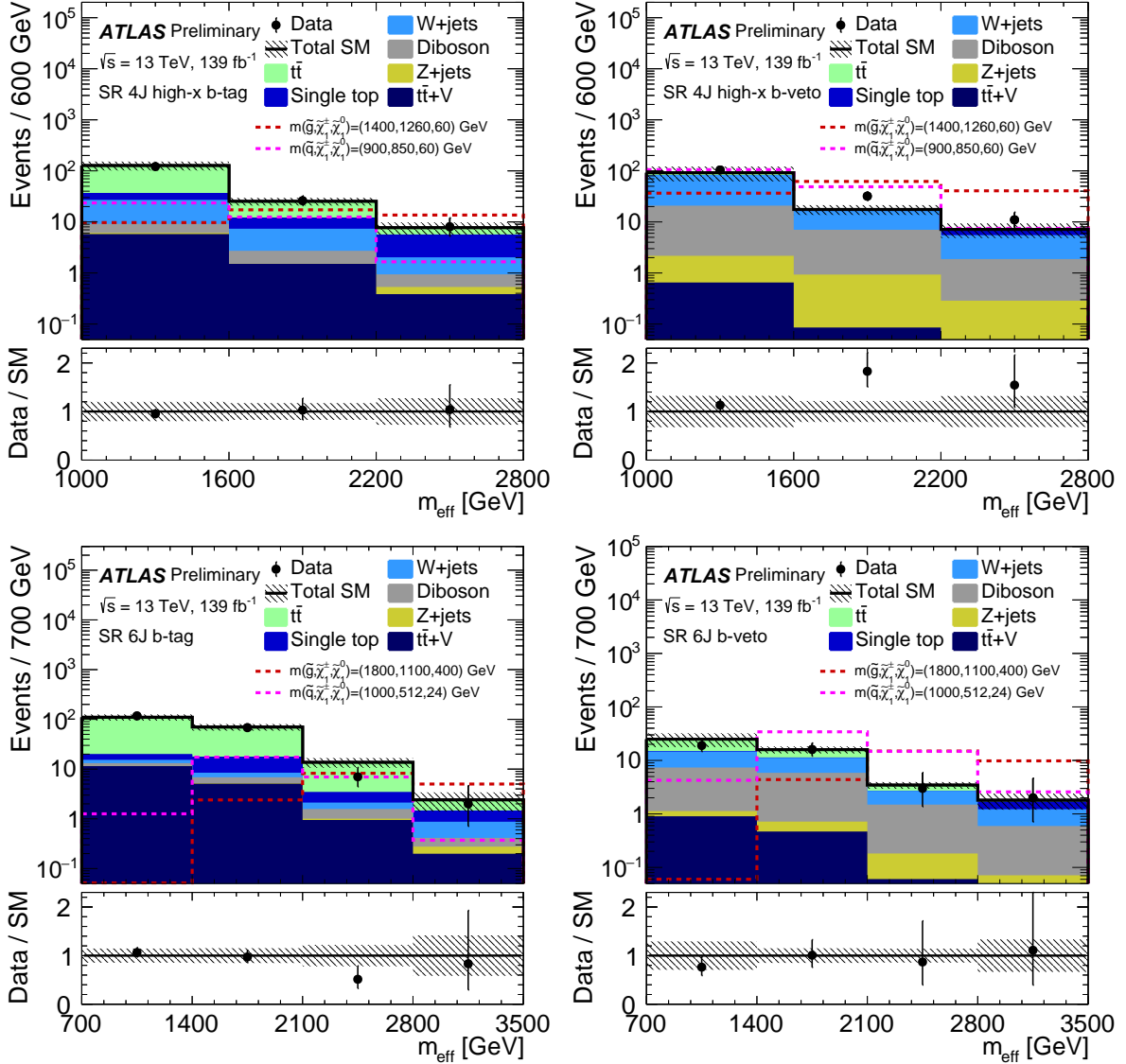


Figure 7: Post-fit m_{eff} distributions in the exclusion 4J high- x and 6J signal regions. The uncertainty bands include all statistical and systematic uncertainties. The dashed lines represent benchmark signal points. Overflow events are included in the last bin.

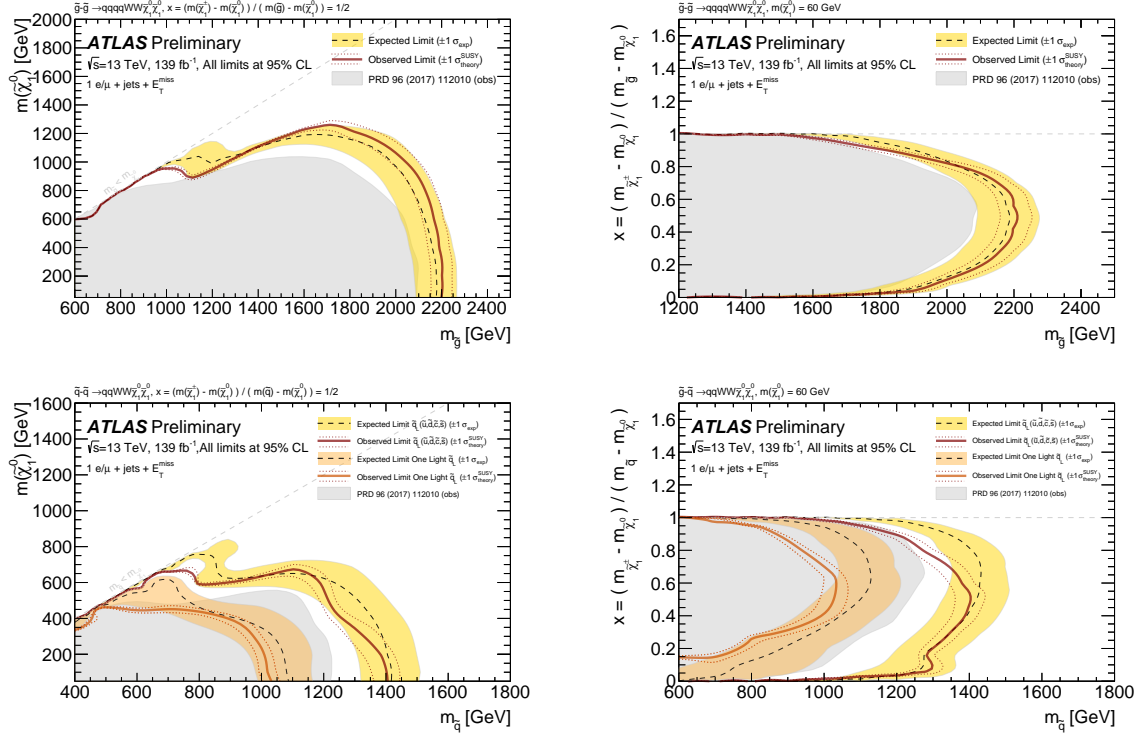


Figure 8: Exclusion contours for gluino one-step $x = 1/2$ (top left), gluino one-step variable- x (top right), squark one-step $x = 1/2$ (bottom left) and squark one-step variable- x (bottom right) scenarios. The orange solid and the dashed lines show the squark one-step $x = 1/2$ (left) and squark one-step variable- x (right) scenarios with the one-flavour scheme. The red solid line corresponds to the observed limit with the red dotted lines indicating the $\pm 1\sigma$ variation of this limit due to the effect of theoretical scale and PDF uncertainties in the signal cross-section. The dark gray dashed line indicates the expected limit with the yellow band representing the $\pm 1\sigma$ variation of the median expected limit due to the experimental and theoretical uncertainties. For reference, exclusion bounds from previous searches with 36.1 fb^{-1} at 13 TeV center-of-mass energy [23] are overlaid by the gray area (the observed limit is shown by the solid line, while the dashed line shows the expected limit).

9 Conclusion

A search for gluinos and squarks in events with one isolated lepton, jets and missing transverse momentum is presented. The analysis uses 139 fb^{-1} of proton–proton collision data collected at a centre-of-mass energy of 13 TeV at the LHC. Four signal regions requiring at least two to six jets are used to cover a broad spectrum of the targeted SUSY model parameter space. While three signal regions are based on high p_T lepton selections and target models with large mass differences between the supersymmetric particles, one dedicated low p_T lepton region is designed to enhance the sensitivity to models with compressed mass spectra. The data agree with the Standard Model background prediction in the signal regions. No significant deviation from the expected Standard Model background is observed. For all signal regions, limits on the visible cross-section are derived in models of new physics within the kinematic requirements of this search. In addition, exclusion limits are placed on models with gluino/squark production and subsequent decays via an intermediate chargino to the lightest neutralino. The exclusion limits of previous searches conducted in early LHC Run 2 are significantly extended. Gluino (Squark) masses up to around 2.2 (1.4) TeV are excluded for a low neutralino mass, while for scenarios with one-flavour scheme, the squark masses up to around 1 TeV are excluded.

References

- [1] ATLAS Collaboration, *Observation of a new particle in the search for the Standard Model Higgs boson with the ATLAS detector at the LHC*, *Phys. Lett. B* **716** (2012) 1, arXiv: [1207.7214 \[hep-ex\]](https://arxiv.org/abs/1207.7214) (cit. on p. 2).
- [2] CMS Collaboration, *Observation of a new boson at a mass of 125 GeV with the CMS experiment at the LHC*, *Phys. Lett. B* **716** (2012) 30, arXiv: [1207.7235 \[hep-ex\]](https://arxiv.org/abs/1207.7235) (cit. on p. 2).
- [3] ATLAS and CMS Collaborations, *Combined Measurement of the Higgs Boson Mass in pp Collisions at $\sqrt{s} = 7$ and 8 TeV with the ATLAS and CMS Experiments*, *Phys. Rev. Lett.* **114** (2015) 191803, arXiv: [1503.07589 \[hep-ex\]](https://arxiv.org/abs/1503.07589) (cit. on p. 2).
- [4] ATLAS and CMS Collaborations, *Measurements of the Higgs boson production and decay rates and constraints on its couplings from a combined ATLAS and CMS analysis of the LHC pp collision data at $\sqrt{s} = 7$ and 8 TeV*, *JHEP* **08** (2016) 045, arXiv: [1606.02266 \[hep-ex\]](https://arxiv.org/abs/1606.02266) (cit. on p. 2).
- [5] N. Sakai, *Naturalness in supersymmetric GUTS*, *Z. Phys. C* **11** (1981) 153 (cit. on p. 2).
- [6] S. Dimopoulos, S. Raby and F. Wilczek, *Supersymmetry and the scale of unification*, *Phys. Rev. D* **24** (1981) 1681 (cit. on p. 2).
- [7] L. E. Ibanez and G. G. Ross, *Low-energy predictions in supersymmetric grand unified theories*, *Phys. Lett. B* **105** (1981) 439 (cit. on p. 2).
- [8] S. Dimopoulos and H. Georgi, *Softly broken supersymmetry and SU(5)*, *Nucl. Phys. B* **193** (1981) 150 (cit. on p. 2).
- [9] Y. A. Golfand and E. P. Likhtman, *Extension of the Algebra of Poincare Group Generators and Violation of P invariance*, *JETP Lett.* **13** (1971) 323, [*Pisma Zh. Eksp. Teor. Fiz.* **13** (1971) 452] (cit. on p. 2).
- [10] D. V. Volkov and V. P. Akulov, *Is the neutrino a goldstone particle?*, *Phys. Lett. B* **46** (1973) 109 (cit. on p. 2).
- [11] J. Wess and B. Zumino, *Supergauge transformations in four-dimensions*, *Nucl. Phys. B* **70** (1974) 39 (cit. on p. 2).
- [12] J. Wess and B. Zumino, *Supergauge invariant extension of quantum electrodynamics*, *Nucl. Phys. B* **78** (1974) 1 (cit. on p. 2).
- [13] S. Ferrara and B. Zumino, *Supergauge invariant Yang-Mills theories*, *Nucl. Phys. B* **79** (1974) 413 (cit. on p. 2).
- [14] A. Salam and J. A. Strathdee, *Super-symmetry and non-Abelian gauges*, *Phys. Lett. B* **51** (1974) 353 (cit. on p. 2).
- [15] G. R. Farrar and P. Fayet, *Phenomenology of the production, decay, and detection of new hadronic states associated with supersymmetry*, *Phys. Lett. B* **76** (1978) 575 (cit. on p. 2).
- [16] H. Goldberg, *Constraint on the Photino Mass from Cosmology*, *Phys. Rev. Lett.* **50** (1983) 1419, [Erratum: *Phys. Rev. Lett.* **103** (2009) 099905] (cit. on p. 2).
- [17] J. R. Ellis, J. S. Hagelin, D. V. Nanopoulos, K. A. Olive and M. Srednicki, *Supersymmetric relics from the big bang*, *Nucl. Phys. B* **238** (1984) 453 (cit. on p. 2).
- [18] P. Fayet, *Supersymmetry and Weak, Electromagnetic and Strong Interactions*, *Phys. Lett. B* **64** (1976) 159 (cit. on p. 2).

[19] P. Fayet, *Spontaneously broken supersymmetric theories of weak, electromagnetic and strong interactions*, *Phys. Lett. B* **69** (1977) 489 (cit. on p. 2).

[20] J. Alwall, P. Schuster and N. Toro, *Simplified models for a first characterization of new physics at the LHC*, *Phys. Rev. D* **79** (2009) 075020, arXiv: [0810.3921 \[hep-ph\]](#) (cit. on p. 2).

[21] D. Alves et al., *Simplified models for LHC new physics searches*, *J. Phys. G* **39** (2012) 105005, arXiv: [1105.2838 \[hep-ph\]](#) (cit. on p. 2).

[22] ATLAS Collaboration, *Further search for supersymmetry at $\sqrt{s} = 7$ TeV in final states with jets, missing transverse momentum and isolated leptons with the ATLAS detector*, *Phys. Rev. D* **86** (2012) 092002, arXiv: [1208.4688 \[hep-ex\]](#) (cit. on p. 2).

[23] ATLAS Collaboration, *Search for squarks and gluinos in events with an isolated lepton, jets, and missing transverse momentum at $\sqrt{s} = 13$ TeV with the ATLAS detector*, *Phys. Rev. D* **96** (2017) 112010, arXiv: [1708.08232 \[hep-ex\]](#) (cit. on pp. 3, 23).

[24] CMS Collaboration, *Search for supersymmetry in events with one lepton and multiple jets in proton–proton collisions at $\sqrt{s} = 13$ TeV*, *Phys. Rev. D* **95** (2017) 012011, arXiv: [1609.09386 \[hep-ex\]](#) (cit. on p. 3).

[25] CMS Collaboration, *Search for supersymmetry in multijet events with missing transverse momentum in proton–proton collisions at 13 TeV*, *Phys. Rev. D* **96** (2017) 032003, arXiv: [1704.07781 \[hep-ex\]](#) (cit. on p. 3).

[26] ATLAS Collaboration, *The ATLAS Experiment at the CERN Large Hadron Collider*, *JINST* **3** (2008) S08003 (cit. on p. 3).

[27] ATLAS Collaboration, *ATLAS Insertable B-Layer Technical Design Report*, ATLAS-TDR-19, 2010, URL: <https://cds.cern.ch/record/1291633>, *ATLAS Insertable B-Layer Technical Design Report Addendum*, ATLAS-TDR-19-ADD-1, 2012, URL: <https://cds.cern.ch/record/1451888> (cit. on p. 3).

[28] B. Abbott et al., *Production and integration of the ATLAS Insertable B-Layer*, *JINST* **13** (2018) T05008, arXiv: [1803.00844 \[physics.ins-det\]](#) (cit. on p. 3).

[29] ATLAS Collaboration, *Performance of the ATLAS trigger system in 2015*, *Eur. Phys. J. C* **77** (2017) 317, arXiv: [1611.09661 \[hep-ex\]](#) (cit. on p. 3).

[30] ATLAS Collaboration, *Luminosity determination in pp collisions at $\sqrt{s} = 13$ TeV using the ATLAS detector at the LHC*, ATLAS-CONF-2019-021, 2019, URL: <https://cds.cern.ch/record/2677054> (cit. on p. 4).

[31] G. Avoni et al., *The new LUCID-2 detector for luminosity measurement and monitoring in ATLAS*, *JINST* **13** (2018) P07017 (cit. on p. 4).

[32] ATLAS Collaboration, *The simulation principle and performance of the ATLAS fast calorimeter simulation FastCaloSim*, ATL-PHYS-PUB-2010-013, 2010, URL: <https://cds.cern.ch/record/1300517> (cit. on p. 4).

[33] ATLAS Collaboration, *The ATLAS Simulation Infrastructure*, *Eur. Phys. J. C* **70** (2010) 823, arXiv: [1005.4568 \[physics.ins-det\]](#) (cit. on p. 4).

[34] S. Agostinelli et al., *GEANT4 - a simulation toolkit*, *Nucl. Instrum. Meth. A* **506** (2003) 250 (cit. on p. 4).

[35] T. Sjöstrand, S. Mrenna and P. Z. Skands, *A brief introduction to PYTHIA 8.1*, *Comput. Phys. Commun.* **178** (2008) 852, arXiv: [0710.3820 \[hep-ph\]](#) (cit. on p. 4).

[36] R. D. Ball et al., *Parton distributions with LHC data*, *Nucl. Phys. B* **867** (2013) 244, arXiv: [1207.1303 \[hep-ph\]](https://arxiv.org/abs/1207.1303) (cit. on pp. 4, 5).

[37] ATLAS Collaboration, *The Pythia 8 A3 tune description of ATLAS minimum bias and inelastic measurements incorporating the Donnachie–Landshoff diffractive model*, ATL-PHYS-PUB-2016-017, 2016, URL: <https://cds.cern.ch/record/2206965> (cit. on p. 4).

[38] W. Beenakker, C. Borschensky, M. Krämer, A. Kulesza and E. Laenen, *NNLL-fast: predictions for coloured supersymmetric particle production at the LHC with threshold and Coulomb resummation*, *JHEP* **12** (2016) 133, arXiv: [1607.07741 \[hep-ph\]](https://arxiv.org/abs/1607.07741) (cit. on p. 4).

[39] W. Beenakker et al., *NNLL Resummation for Squark-Antisquark and Gluino-Pair Production at the LHC*, *JHEP* **12** (2014) 023, arXiv: [1404.3134 \[hep-ph\]](https://arxiv.org/abs/1404.3134) (cit. on p. 4).

[40] W. Beenakker et al., *Towards NNLL resummation: hard matching coefficients for squark and gluino hadroproduction*, *JHEP* **10** (2013) 120, arXiv: [1304.6354 \[hep-ph\]](https://arxiv.org/abs/1304.6354) (cit. on p. 4).

[41] W. Beenakker et al., *NNLL resummation for squark-antisquark pair production at the LHC*, *JHEP* **01** (2012) 076, arXiv: [1110.2446 \[hep-ph\]](https://arxiv.org/abs/1110.2446) (cit. on p. 4).

[42] W. Beenakker, S. Brensing, M. Kramer, A. Kulesza, E. Laenen et al., *Soft-gluon resummation for squark and gluino hadroproduction*, *JHEP* **0912** (2009) 041, arXiv: [0909.4418 \[hep-ph\]](https://arxiv.org/abs/0909.4418) (cit. on p. 4).

[43] A. Kulesza and L. Motyka, *Soft gluon resummation for the production of gluino-gluino and squark-antisquark pairs at the LHC*, *Phys.Rev. D* **80** (2009) 095004, arXiv: [0905.4749 \[hep-ph\]](https://arxiv.org/abs/0905.4749) (cit. on p. 4).

[44] A. Kulesza and L. Motyka, *Threshold resummation for squark-antisquark and gluino-pair production at the LHC*, *Phys.Rev.Lett.* **102** (2009) 111802, arXiv: [0807.2405 \[hep-ph\]](https://arxiv.org/abs/0807.2405) (cit. on p. 4).

[45] W. Beenakker, R. Hopker, M. Spira and P. Zerwas, *Squark and gluino production at hadron colliders*, *Nucl.Phys. B* **492** (1997) 51, arXiv: [hep-ph/9610490 \[hep-ph\]](https://arxiv.org/abs/hep-ph/9610490) (cit. on p. 4).

[46] J. Butterworth et al., *PDF4LHC recommendations for LHC Run II*, *J. Phys. G* **43** (2016) 023001, arXiv: [1510.03865 \[hep-ph\]](https://arxiv.org/abs/1510.03865) (cit. on pp. 4, 14).

[47] T. Gleisberg and S. Höche, *Comix, a new matrix element generator*, *JHEP* **12** (2008) 039, arXiv: [0808.3674 \[hep-ph\]](https://arxiv.org/abs/0808.3674) (cit. on p. 4).

[48] F. Caccioli, P. Maierhöfer and S. Pozzorini, *Scattering Amplitudes with Open Loops*, *Phys. Rev. Lett.* **108** (2012) 111601, arXiv: [1111.5206 \[hep-ph\]](https://arxiv.org/abs/1111.5206) (cit. on p. 4).

[49] A. Denner, S. Dittmaier and L. Hofer, *Collier: A fortran-based complex one-loop library in extended regularizations*, *Comput. Phys. Commun.* **212** (2017) 220, arXiv: [1604.06792 \[hep-ph\]](https://arxiv.org/abs/1604.06792) (cit. on p. 4).

[50] S. Schumann and F. Krauss, *A parton shower algorithm based on Catani–Seymour dipole factorisation*, *JHEP* **03** (2008) 038, arXiv: [0709.1027 \[hep-ph\]](https://arxiv.org/abs/0709.1027) (cit. on p. 4).

[51] S. Höche, F. Krauss, M. Schönherr and F. Siegert, *A critical appraisal of NLO+PS matching methods*, *JHEP* **09** (2012) 049, arXiv: [1111.1220 \[hep-ph\]](https://arxiv.org/abs/1111.1220) (cit. on p. 4).

[52] S. Höche, F. Krauss, M. Schönherr and F. Siegert, *QCD matrix elements + parton showers. The NLO case*, *JHEP* **04** (2013) 027, arXiv: [1207.5030 \[hep-ph\]](https://arxiv.org/abs/1207.5030) (cit. on p. 4).

[53] S. Catani, F. Krauss, R. Kuhn and B. R. Webber, *QCD Matrix Elements + Parton Showers*, *JHEP* **11** (2001) 063, arXiv: [hep-ph/0109231](https://arxiv.org/abs/hep-ph/0109231) (cit. on p. 4).

[54] S. Höche, F. Krauss, S. Schumann and F. Siegert, *QCD matrix elements and truncated showers*, *JHEP* **05** (2009) 053, arXiv: [0903.1219 \[hep-ph\]](#) (cit. on p. 4).

[55] D. J. Lange, *The EvtGen particle decay simulation package*, *Nucl. Instrum. Meth. A* **462** (2001) 152 (cit. on p. 5).

[56] L. Lönnblad and S. Prestel, *Merging multi-leg NLO matrix elements with parton showers*, *JHEP* **03** (2013) 166, arXiv: [1211.7278 \[hep-ph\]](#) (cit. on p. 5).

[57] S. Alioli, P. Nason, C. Oleari and E. Re, *A general framework for implementing NLO calculations in shower Monte Carlo programs: the POWHEG BOX*, *JHEP* **06** (2010) 043, arXiv: [1002.2581 \[hep-ph\]](#) (cit. on p. 5).

[58] S. Frixione, P. Nason and C. Oleari, *Matching NLO QCD computations with parton shower simulations: the POWHEG method*, *JHEP* **11** (2007) 070, arXiv: [0709.2092 \[hep-ph\]](#) (cit. on p. 5).

[59] S. Frixione, P. Nason and G. Ridolfi, *A positive-weight next-to-leading-order Monte Carlo for heavy flavour hadroproduction*, *JHEP* **09** (2007) 126, arXiv: [0707.3088 \[hep-ph\]](#) (cit. on p. 5).

[60] P. Nason, *A new method for combining NLO QCD with shower Monte Carlo algorithms*, *JHEP* **11** (2004) 040, arXiv: [hep-ph/0409146](#) (cit. on p. 5).

[61] T. Sjöstrand et al., *An introduction to PYTHIA 8.2*, *Computer Physics Communications* **191** (2015) 159, ISSN: 0010-4655, URL: <http://www.sciencedirect.com/science/article/pii/S0010465515000442> (cit. on p. 5).

[62] ATLAS Collaboration, *ATLAS Pythia 8 tunes to 7 TeV data*, ATL-PHYS-PUB-2014-021, 2014, URL: <https://cds.cern.ch/record/1966419> (cit. on p. 5).

[63] M. Czakon and A. Mitov, *Top++: A program for the calculation of the top-pair cross-section at hadron colliders*, *Comput. Phys. Commun.* **185** (2014) 2930, arXiv: [1112.5675 \[hep-ph\]](#) (cit. on p. 5).

[64] E. Re, *Single-top Wt-channel production matched with parton showers using the POWHEG method*, *Eur. Phys. J. C* **71** (2011) 1547, arXiv: [1009.2450 \[hep-ph\]](#) (cit. on p. 5).

[65] R. Frederix, E. Re and P. Torrielli, *Single-top t-channel hadroproduction in the four-flavour scheme with POWHEG and aMC@NLO*, *JHEP* **09** (2012) 130, arXiv: [1207.5391 \[hep-ph\]](#) (cit. on p. 5).

[66] S. Alioli, P. Nason, C. Oleari and E. Re, *NLO single-top production matched with shower in POWHEG: s- and t-channel contributions*, *JHEP* **09** (2009) 111, [Erratum: JHEP02,011(2010)], arXiv: [0907.4076 \[hep-ph\]](#) (cit. on p. 5).

[67] M. Aliev et al., *HATHOR – HAdronic Top and Heavy quarks crOss section calculatoR*, *Comput. Phys. Commun.* **182** (2011) 1034, arXiv: [1007.1327 \[hep-ph\]](#) (cit. on p. 5).

[68] T. Gleisberg et al., *Event generation with SHERPA 1.1*, *JHEP* **02** (2009) 007, arXiv: [0811.4622 \[hep-ph\]](#) (cit. on p. 5).

[69] C. Anastasiou, L. J. Dixon, K. Melnikov and F. Petriello, *High precision QCD at hadron colliders: Electroweak gauge boson rapidity distributions at NNLO*, *Phys. Rev. D* **69** (2004) 094008, arXiv: [hep-ph/0312266](#) (cit. on p. 5).

[70] P. Bärnreuther, M. Czakon and A. Mitov, *Percent Level Precision Physics at the Tevatron: First Genuine NNLO QCD Corrections to $q\bar{q} \rightarrow t\bar{t} + X$* , *Phys. Rev. Lett.* **109** (2012) 132001, arXiv: [1204.5201 \[hep-ph\]](#) (cit. on p. 5).

[71] ATLAS Collaboration, *Vertex Reconstruction Performance of the ATLAS Detector at $\sqrt{s} = 13$ TeV*, ATL-PHYS-PUB-2015-026, 2015, URL: <https://cds.cern.ch/record/2037717> (cit. on p. 5).

[72] ATLAS Collaboration, *Selection of jets produced in 13 TeV proton–proton collisions with the ATLAS detector*, ATLAS-CONF-2015-029, 2015, URL: <https://cds.cern.ch/record/2037702> (cit. on p. 5).

[73] ATLAS Collaboration, *Electron and photon performance measurements with the ATLAS detector using the 2015–2017 LHC proton–proton collision data*, JINST **14** (2019) P12006, arXiv: [1908.00005 \[hep-ex\]](https://arxiv.org/abs/1908.00005) (cit. on pp. 5, 14).

[74] ATLAS Collaboration, *Muon reconstruction performance of the ATLAS detector in proton–proton collision data at $\sqrt{s} = 13$ TeV*, Eur. Phys. J. C **76** (2016) 292, arXiv: [1603.05598 \[hep-ex\]](https://arxiv.org/abs/1603.05598) (cit. on pp. 5, 6, 14).

[75] ATLAS Collaboration, *Topological cell clustering in the ATLAS calorimeters and its performance in LHC Run 1*, Eur. Phys. J. C **77** (2017) 490, arXiv: [1603.02934 \[hep-ex\]](https://arxiv.org/abs/1603.02934) (cit. on p. 6).

[76] M. Cacciari, G. P. Salam and G. Soyez, *The anti- k_t jet clustering algorithm*, JHEP **04** (2008) 063, arXiv: [0802.1189 \[hep-ph\]](https://arxiv.org/abs/0802.1189) (cit. on p. 6).

[77] ATLAS Collaboration, *Performance of pile-up mitigation techniques for jets in pp collisions at $\sqrt{s} = 8$ TeV using the ATLAS detector*, Eur. Phys. J. C **76** (2016) 581, arXiv: [1510.03823 \[hep-ex\]](https://arxiv.org/abs/1510.03823) (cit. on p. 6).

[78] M. Cacciari, G. P. Salam and G. Soyez, *FastJet user manual*, Eur. Phys. J. C **72** (2012) 1896, arXiv: [1111.6097 \[hep-ph\]](https://arxiv.org/abs/1111.6097) (cit. on p. 6).

[79] ATLAS Collaboration, *ATLAS b -jet identification performance and efficiency measurement with $t\bar{t}$ events in pp collisions at $\sqrt{s} = 13$ TeV*, Eur. Phys. J. C **79** (2019) 970, arXiv: [1907.05120 \[hep-ex\]](https://arxiv.org/abs/1907.05120) (cit. on pp. 6, 14).

[80] ATLAS Collaboration, *Optimisation and performance studies of the ATLAS b -tagging algorithms for the 2017-18 LHC run*, ATL-PHYS-PUB-2017-013, 2017, URL: <https://cds.cern.ch/record/2273281> (cit. on p. 6).

[81] M. Cacciari, G. P. Salam and G. Soyez, *The catchment area of jets*, JHEP **04** (2008) 005, arXiv: [0802.1188 \[hep-ph\]](https://arxiv.org/abs/0802.1188) (cit. on p. 6).

[82] ATLAS Collaboration, *Measurement of the photon identification efficiencies with the ATLAS detector using LHC Run 2 data collected in 2015 and 2016*, Eur. Phys. J. C **79** (2019) 205, arXiv: [1810.05087 \[hep-ex\]](https://arxiv.org/abs/1810.05087) (cit. on p. 6).

[83] ATLAS Collaboration, *Performance of missing transverse momentum reconstruction with the ATLAS detector using proton–proton collisions at $\sqrt{s} = 13$ TeV*, Eur. Phys. J. C **78** (2018) 903, arXiv: [1802.08168 \[hep-ex\]](https://arxiv.org/abs/1802.08168) (cit. on p. 6).

[84] ATLAS Collaboration, *E_T^{miss} performance in the ATLAS detector using 2015–2016 LHC pp collisions*, ATLAS-CONF-2018-023, 2018, URL: <https://cds.cern.ch/record/2625233> (cit. on p. 6).

[85] ATLAS Collaboration, *Performance of the missing transverse momentum triggers for the ATLAS detector during Run-2 data taking*, JHEP (2019) 51, arXiv: [2005.09554 \[hep-ex\]](https://arxiv.org/abs/2005.09554) (cit. on p. 6).

[86] C. Chen, *New approach to identifying boosted hadronically decaying particles using jet substructure in its center-of-mass frame*, Phys. Rev. D **85** (2012) 034007, arXiv: [1112.2567 \[hep-ph\]](https://arxiv.org/abs/1112.2567) (cit. on p. 7).

- [87] J. Bellm et al., *Herwig 7.0/Herwig++ 3.0 release note*, *Eur. Phys. J.* **C76** (2016) 196, arXiv: [1512.01178 \[hep-ph\]](https://arxiv.org/abs/1512.01178) (cit. on p. 13).
- [88] ATLAS Collaboration, *Simulation of top-quark production for the ATLAS experiment at $\sqrt{s} = 13$ TeV*, ATL-PHYS-PUB-2016-004, 2016, URL: <https://cds.cern.ch/record/2120417> (cit. on p. 13).
- [89] ATLAS Collaboration, *Jet energy scale measurements and their systematic uncertainties in proton–proton collisions at $\sqrt{s} = 13$ TeV with the ATLAS detector*, *Phys. Rev. D* **96** (2017) 072002, arXiv: [1703.09665 \[hep-ex\]](https://arxiv.org/abs/1703.09665) (cit. on p. 14).
- [90] ATLAS Collaboration, *Calibration of the b-tagging efficiency on charm jets using a sample of $W + c$ events with $\sqrt{s} = 13$ TeV ATLAS data*, ATLAS-CONF-2018-055, 2018, URL: <https://cds.cern.ch/record/2652195> (cit. on p. 14).
- [91] ATLAS Collaboration, *Calibration of light-flavour b-jet mistagging rates using ATLAS proton–proton collision data at $\sqrt{s} = 13$ TeV*, ATLAS-CONF-2018-006, 2018, URL: <https://cds.cern.ch/record/2314418> (cit. on p. 15).
- [92] M. Baak et al., *HistFitter software framework for statistical data analysis*, *Eur. Phys. J. C* **75** (2015) 153, arXiv: [1410.1280 \[hep-ex\]](https://arxiv.org/abs/1410.1280) (cit. on p. 15).
- [93] A. L. Read, *Presentation of search results: The CL_S technique*, *J. Phys. G* **28** (2002) 2693 (cit. on p. 16).